Polarization control of epitaxial barium titanate ($BaTiO_3$) grown by Pulsed-Laser Deposition on a MBE-$SrTiO_3$/Si(001) pseudo-substrate

Tsang-Hsuan Wang[1,2,*], Po-Chun (Brent) Hsu[1,3], Maxim Korytov[1], Jan Genoe[1,2] and Clement Merckling[1]

1: Imec, Kapeldreef 75, B-3001 Leuven, Belgium

2: ESAT Department, KU Leuven, Kasteelpark Arenberg 10, B-3001 Leuven, Belgium

3: Department of Materials Engineering, KU Leuven, Kasteelpark Arenberg 44, B-3001 Leuven, Belgium

*e-mail: tsang.hsuan.wang@imec.be

Keywords

Barium titanate, pulsed-laser deposition, polarization, nano-beam diffraction, C-V characterization

Accepted

Abstract

Barium titanate ($BaTiO_3$ or BTO) is a perovskite structure material with interesting intrinsic properties such as spontaneous ferroelectricity or electro-optical behavior that strongly depends on thin film crystallinity. For such functional oxide systems, the Pulsed-Laser Deposition (PLD) approach is one promising growth technique due to its precise stoichiometry control of the metals composing the perovskite crystal and higher oxygen environment compared to the classically used Molecular Beam Epitaxy (MBE) approach. In this article, we demonstrate a BTO epitaxial layer by PLD onto Si(001) substrate thanks to a thin pseudomorphic $SrTiO_3$ buffer layer grown by MBE. In our study, the various investigated PLD parameters show strong impacts on the BTO polarization orientation. Hence, adjusting the growth conditions allows control of the polarization orientation, which is crucial for both electronic and optical applications. In addition, lattice parameter changes of BTO layers are investigated using X-Ray Diffraction (XRD) and cross-section Transmission Electron Microscopy (TEM),

which evidenced a correlation between mismatch relaxation and oxygen growth pressure. Finally, with the analysis of BTO C-V curves, the polarization direction transition is demonstrated electrically.

Introduction

Perovskite-based oxide materials are widely studied due to their extensive applications in nanoelectronic, opto-electronic, and electro-mechanic devices[1–5]. Among these, barium titanate ($BaTiO_3$ or BTO) attracts attention due to its strong spontaneous ferroelectricity and notable strong electro-optical properties[6–8]. At room temperature, $BaTiO_3$ bulk has a tetragonal crystal symmetry[7,9]. Upon applying electric field, the displacement of the titanium atom along the polarization direction generates ferroelectricity and other intriguing properties[8,10,11]. In order to enhance ferroelectric behavior, a single-domain BTO layer is required[12,13].

BTO thin films with the elongated axis perpendicular to the substrate surface is named c-oriented BTO (c-BTO), while BTO thin films with the elongated axis lying parallel to the substrate surface is named a-oriented BTO (a-BTO). For memory or low-power switching applications, the c-BTO orientation is preferred due to ease of fabrication and device design[14,15]. However, for electro-optical applications, a-BTO orientation is more effective than c-BTO due to its larger Pockels coefficients in such configuration. As in Pockels tensor of BTO, the largest coefficient is r_{51}, which is at least 1 order larger than other tensor items[16]. For more prominent Pockels effect, the applied electric field must lie in the same plane as optical axis, which can only be achieved by having a-oriented BTO[17]. As a result, controlling the BTO orientation during the epitaxy process is crucial[18,19].

For integration of these functional oxides onto silicon substrates, the main technique used for the epitaxy of such oxide thin films are molecular beam epitaxy (MBE)[20–22] and pulsed-laser deposition (PLD)[23–25]. MBE is suitable for epitaxial growth due to its slow growth rate and in-situ Reflection High-energy Electron Diffraction (RHEED) monitoring. Using MBE, epitaxial growth is achieved by precise control of atomic growth. However, the limited oxygen environment of maximum 10^{-5} mbar favors the formation of oxygen vacancies in the BTO layer[26], which significantly influence both electrical and

Accepted

optical properties[27–29]. To reduce the undesirable impact of oxygen vacancies, post-growth annealing at high temperature and especially under high oxygen pressure are needed[30,31]. However, high temperature annealing results in generally strong interfacial reactions with Silicon substrates[32,33]. Compared to MBE technique, PLD can reach higher oxygen pressure of above 10^{-2} mbar based on a different epitaxial process system, including the usage of ceramic target and plasma plume formation between target and substrate, giving a very interesting alternative approach for complex oxide epitaxy. Nevertheless, the direct epitaxy of oxides on Si substrate by PLD is still a challenge due to the higher O_2 pressure, which results in amorphous SiO_2 interface formation, and lack of atomic control[34]. Until today, there's only one group that had successfully demonstrated the epitaxial growth of strontium titanate on top of Si(001) substrates using PLD, showing the difficulty of a whole-PLD epitaxial heterostructure[35]. To integrate functional oxides on Si substrate, we then combine these two techniques by using MBE-grown strontium titanate ($SrTiO_3$ or STO) onto Si substrate as a template[36], followed by a subsequent BTO layer growth with ex-situ PLD. In this way, we combined the advantages of PLD in stoichiometry and high O_2 pressure together with MBE for the monolithic integration on Si.

Due to the 2 % larger lattice parameter compared with STO, the epitaxially grown BTO is initially compressively strained[36,37], which results in elongation of the BTO out-of-plane lattice parameter and hence favorizes c-BTO growth. Plastic relaxations occurring beyond a critical thickness modify BTO lattice parameters and may impact BTO polarization orientation. In this study, lattice mismatch relaxation behavior inside BTO film is shown to be closely correlated with PLD parameters, indicating the capability to control the BTO polarization via these growth parameters.

Experimental

The 10-nm-STO buffer layers were grown on 8-inch Si(001) substrate using Riber 49 200mm MBE cluster system. The detailed processes were previously reported[36,38]. Once we obtained a single-crystalline STO layer, the wafer was then diced into smaller pieces of 3.8×3.8 cm^2. Note all BTO films were grown on the same STO batch template to reduce the substrate fluctuation and to strengthen

Accepted

PLD parameter effects. All BTO films were grown in a Solmates 200mm production PLD system equipped with a KrF laser and a BTO ceramic target source (99.9%) from Neyco. After introducing the STO / Si samples, the chamber was pumped down to base pressure at around 10^{-4} mbar; then the sample holder was heated above 650 ˚C under oxygen ambient before turning on laser power. During temperature ramping and the subsequent BTO growth, oxygen gas was introduced, ranging from 0.01 mbar to 0.05 mbar. We confirmed STO template stability by comparing XRD peak position and intensity after the 750 ˚C and low-pressure environment in PLD process. The thickness of all BTO films was kept at around 100 nm +/- 10 nm as measured by X-Ray Reflectivity (XRR) analysis. In such analysis, the film thickness was determined by the Fourier transform peak position of the acquired curve.

The epitaxial film crystal quality was further assessed by X-ray diffraction (XRD) for structural analyses. Lattice parameters were calculated by symmetric (002) as well as asymmetric (202) and (022) scans using Bragg's law. Crystal mosaicity can be analyzed by performing ω-scan of XRD analysis. We used full width at half maximum (FWHM) value of (002) peak by ω-scan to compare epitaxial film quality. The 10 nm STO buffer layer showed good crystallinity with FWHM of 0.2˚- 0.3˚. In-plane and out-of-plane lattice parameters distributions were measured with Nano-Beam Diffraction (NBD) using a double-corrected Titan G2 60-300 transmission electron microscope operating at 200 kV. NBD consists of scanning a region of interest with an almost parallel nanometer-size electron beam and acquiring a diffraction pattern in every point[39]. Distribution of the local lattice parameter is then calculated by comparing the diffraction patterns acquired in the region of interest with a pattern acquired in a reference unstrained area[40]. Strain distribution in the two directions perpendicular to the electron beam can be measured with a precision up to 0.1 %[41]. Surface roughness was measured by atomic force microscopy (AFM) using Bruker Dimension Edge. C-V measurement was carried out using Agilent E4980A from 1k Hz to 1M Hz and I-V measurement using Agilent B1500A for electrical properties analyses.

Results

Accepted

Growth rate is one of the most crucial parameters to influence the crystalline quality for an epitaxially-grown thin film. In PLD system, growth rate is principally controlled by laser parameters. When the laser beam hits the ceramic target, the heat induced by the high energy laser melts and ablates the materials. The ablated materials include ions, activated molecules, and electrons, forming a plasma plume between target and substrate surface. These high energy species will then diffuse and crystallize on the substrate surface[42,43]. Pulsed-laser frequency directly influences the growth rate and surface diffusion time, which largely determines the growth mode of thin films, thus is crucial on improving crystallinity of thin films.[44] The lower the laser frequency, the lower the growth rate will be as there are no materials being ablated in between pulses. Different laser frequencies were used for BTO growth. The Figure 1(a) represents the ω-2Θ scans around the BTO(002) Bragg reflection angle with varied growth rate between 0.02 nm/s and 0.1 nm/s. The STO(002) peak signal originates from single-crystalline STO / Si(001) pseudo-substrate. For all samples, a strong peak observed at 44.2˚ corresponds to the (002) diffraction of the tetragonal BTO crystal. However, for the sample with growth rate of 0.1 nm/s, additional peaks located at 41.8˚ and 46.7˚ were found; these peaks are attributed to the orthorhombic crystal structure of BTO and are present in all samples with high growth rate (SI Fig. 1), suggesting the presence of undesired phase by using too large the growth rate. With lower laser repetition rate, the atomic diffusion time of species on the substrate surface is increased, allowing better alignment with the initial STO lattice. Therefore, growth rates below 0.1 nm/s lead to epitaxy of BTO. The epitaxy of BTO is confirmed by BTO(202) and Si(202) ϕ-scans, which showed the 4-fold symmetry and the 45˚ rotation of BTO lattice on top of Si (SI Fig. 7). To further assess the crystallinity of the different growth rates, the ω-scan of BTO(002) was carried out. In the Figure 1(c), the FWHM values of BTO(002) ω-scan were plotted in function of growth rate. It can be clearly seen the crystallinity of BTO films improved as the growth rate reduced with FWHM decreased from around 0.3˚ to 0.25˚.

Epitaxial BTO can be obtained using STO as buffer layer due to their similar crystal structures and lattice parameters. However, this slight differences of +2 % in lattice parameters and +20 % in thermal

Accepted

coefficients produces compressive in-plane strain in BTO epilayer and thus elongates the out-of-plane BTO lattice parameter; on the contrary, the thermal coefficient difference between BTO and Si substrate results in the tensile in-plane strain which shortens the out-of-plane BTO lattice parameter [18,37,45]. As a result, the $BaTiO_3$ grown on $SrTiO_3$ buffer is inherently c-oriented when the thickness is small, and gradually becomes a-oriented dominated when increasing the BTO thickness. To change polarization direction, we need to control the elongated axis orientation, in particular by enabling a faster strain relaxation mechanism in BTO films. The initial compressive strain can be relaxed by increasing BTO thickness, or other processing parameters such as substrate temperature and chamber pressure. By the use of both symmetric and asymmetric XRD scans, we can obtain out-of-plane and in-plane lattice parameters. Upon investigating XRD peak position and the ratio between c- and a-axis, we can know orientation of the dominant BTO polarization axis.

As shown in the Figure 1(b) and (c), increasing substrate temperature not only improved crystallinity but also impacted the out-of-plane lattice parameter of the BTO layer. The BTO peak position had shifted to larger angle with raising temperature. Also, clear shoulder sub-peaks appeared at smaller angle next to the main peak in the higher temperature $BaTiO_3$ case. The dashed and solid lines in the ω-2Θ XRD scan indicate the tetragonal BTO(002) and BTO(200) peak positions, which roughly separate BTO crystal orientations (i.e. polarizations). The real crystal orientations would need to adopt the asymmetric scan results as well.

Compared with the minor shift resulting from substrate temperature effect, the change in oxygen pressure during $BaTiO_3$ epitaxy showed more obvious shift, as indicated in the Figure 2(a). The out-of-plane lattice parameter reduced largely as oxygen pressure increased, which we attribute to a gradual change of dominant polarization from c- to a-BTO. Similar to the temperature effect, shoulder sub-peaks appeared next to BTO(002) main peak. To investigate these shoulder and main peaks, reciprocal space mappings (RSM) around BTO(002) peak were measured and presented in supplementary material (SI Fig. 2). The FWHM of the main diffraction peak increased from 0.25˚ to 0.45˚, indicating

Accepted

raised mosaicity in the BTO layer, as the oxygen pressure increased. The asymmetric shape of BTO(002) peak suggested uneven distribution of strain inside the high oxygen pressure sample, especially the 0.05 mbar BTO film. The change of lattice parameters with varied oxygen pressures showed to have similar conclusion with Lyu et al[46]. However, detailed lattice parameter changes were related to the buffer layer, which will be discussed below based on the XRD and NBD results.

Since the main and sub-peaks around BTO(002) indicated different BTO lattice parameters, we further deconvoluted BTO(002) diffraction peak of each sample and plotted in the Figure 2(b)-(d). Among different oxygen pressure samples, sub-peak positions were kept fixed for the deconvolution, marked with the same number in the Figure 2(b)-(d). Shift of the main-peak position from smaller angle to larger angle represented the out-of-plane lattice parameter evolution. As illustrated in the Figure 2(e), the area percentage of each peak was compared between different oxygen pressure samples. For the 0.01 mbar low oxygen pressure sample, no presence of shoulder peak indicated a uniform-distributed preferentially c-oriented BTO layer with out-of-plane lattice parameter of ~ 4.09 Å. When oxygen pressure increased to 0.025 mbar, only 17 % of the film had the same lattice parameter of 4.09 Å, while the remaining part of the BTO films had smaller out-of-plane lattice parameters of ~ 4.06 Å. We attributed this to a mixed c-BTO and a-BTO. This reduction of the lattice parameter was even more pronounced in 0.05 mbar oxygen pressure conditions, with out-of-plane lattice parameter to be 4.03 Å for almost 60 % of the BTO film. The tetragonality of this 0.05 mbar BTO sample was 0.980, hence we expected that this sample had a dominant a-orientation.

Transmission electron microscopy was used to further investigate the lattice parameter distribution inside the BTO layers grown with different oxygen pressure. Difference of the *a* and *c* lattice constants of the tetragonal BTO unit cell is about 1%, so we employed NBD, which is one of few TEM techniques able to determine such a small variation of the lattice. NBD measured distribution of lattice parameter normalized to a lattice parameter of the reference region. We could not use Si as a reference due to

Accepted

a difference in the lattice orientation of BTO / STO and Si arising from the 45˚ rotation of their lattices[34]. Thus, for the qualitative NBD maps shown in the Figure 3(a)-(c), we used BTO as a reference region.

Distribution of the in-plane lattice parameter of 3 samples was quite different (Figure 3(a)-(c)). The sample grown with the lower O_2 pressure (Figure 3(a)) showed 50-100 nm wide domains. Medium O_2 pressure sample was composed of 30-50 nm wide domains, while the sample grown with higher O_2 pressure showed very tiny domain structure. These observations were in agreement with the sample surface morphology measured by AFM (Figure 3(d)-(f)), which revealed mosaic structure in all 3 samples with lower O_2 pressure sample showing the largest grain size and higher O_2 pressure having the smallest grain size.

The out-of-plane lattice parameter distribution of 3 samples was rather similar (Figure 4(a)-(c)). However, the sample grown with the lowest O_2 pressure (Figure 4(a)) showed a bit more uniform distribution of lattice parameter than that of the sample grown with higher O_2 pressure (Figure 4(c)). Another difference between the samples was an increase of the out-of-plane lattice parameter next to the BTO / STO interface in the samples grown with high and medium O_2 pressure.

For a quantitative comparison of the lattice parameters between different samples, another set of NBD maps was calculated using STO as a reference region. Averaged profiles traced in the growth direction are shown in the Figure 4(d) and (e). In all 3 samples the in-plane lattice parameter was rapidly increasing above the interface, indicating the BTO / STO lattice mismatch was accommodated via the plastic relaxations. We cannot conclude if the BTO layers were fully relaxed or not, but the BTO grown with the lower O_2 pressure had a little bit higher residual strain than 2 other samples, indicating less mismatch relaxation.

The out-of-plane lattice parameter of the sample grown with the lower O_2 pressure did not change with the layer thickness, which was in a good agreement with the XRD data showing one peak (see Figure 2(b)). The sample with the intermediate O_2 pressure had an increased lattice parameter close to the BTO / STO interface and then it gradually decreased, which corresponded to the ω-2Θ scan with

Accepted

2 peaks (see Figure 2(c)). Similar behavior was observed in the 0.05 mbar sample with the only exception that the lattice parameter increased within last 15-20 nm of the BTO layer. We could assign 3 regions of the BTO layers to 3 peaks of ω-2ϴ scan curve with the interfacial region corresponding to the highest 4.09 Å out-of-plane lattice parameter, the central part of the layer corresponding to the lower 4.03 Å lattice parameter and the top part of the layer corresponding to the intermediate lattice parameter 4.06 Å, as measured by XRD. There was also a good agreement between thickness ratio of these layers and the area percentage of different lattice parameter measured by XRD (Figure 2(e)). Interpretation of the XRD and NBD findings will be discussed below.

Electrical characterizations of BTO / STO / p^+Si MOS capacitor were investigated with 10 nm Au deposited as top electrodes. Au electrodes were sputtered and patterned through shadow mask with diameter of 200 µm. Both I-V and C-V measurements were executed with p^+Si substrate grounded and gate voltage swept from negative to positive bias. Different voltage biases ranged from +/- 1 V to +/- 5 V were applied during I-V measurements, as shown in the Figure 5(a). For an applied voltage below 2.5 V, no hysteresis behavior was observed; however, the hysteresis loop started to appear at voltages above 3 V and became more pronounced as the applied bias increased. These hysteresis loops are resulted from ferroelectricity of BTO film, and the poling electric fields of about 500 kV/cm also agree with reported values[47,48].

C-V measurement was sweeping from negative bias to positive bias, with different voltages ranged from +/- 0.5 V to +/- 5 V at 1M Hz frequency. The C-V results showed similar trend as I-V results, i.e., hysteresis behavior became prominent when the voltage bias was larger than 3 V (SI Fig. 3). As shown in the Figure 5(b), counterclockwise hysteresis loops were observed in all the different oxygen pressure samples and was most notable in the 0.01 mbar BTO which showed the largest hysteresis loop. Backward curve showed positive flat-band voltage shift and different capacitance at accumulation/depletion regions compared with forward curve, which can be understood by charge and poling effect in BTO, as illustrated in the Figure 5(c). When the BTO layers were biased with –5 V,

Accepted

the dipoles inside BTO film were polarized up toward the top contact due to large enough of electric field. At the same time the capacitor was at accumulation region with excess positive charges accumulated at the BTO / Si interface. As the bias increased toward zero, the accumulated charges at BTO / Si interface as well as the voltage stressed at BTO decreased, resulting in less polarized-up dipoles inside BTO films until flat-band voltage was reached. After the flat-band voltage, the positive bias drop mainly depleted the p-type silicon, with little voltage change crossing the BTO film. Thus, polarized-up dipoles remained unchanged, and the C-V curve was behaving like normal depleted MOS. However, dipoles were polarized down after +3 V with reversed direction due to a strong inversion layer formation, resulting in even lower capacitance value. To confirm the inversion layer formation, multi-frequency (multi-f) C-V from 1k to 100k Hz were measured and plotted in the insertion of the Figure 5(c). An obvious inversion region formation at ~1k Hz with a fixed value of accumulation capacitance at full range of frequency can be clearly observed, which was consistent to a multi-f CV-curve of a normal p-Si MOS capacitor. A more detailed result and explanation of multi-f C-V hysteresis can be found in SI Fig. 4. Based on the results, a dotted line in the schematics indicated the low frequency curve, in comparison with the solid line for C-V curve at 1M Hz. For backward curve, similar but reverse poling direction inside BTO films resulted in the shift of flat-band voltage and the capacitance difference. When the applied voltage was smaller than –3 V, dipoles were again polarized-up reversely and lowered the accumulation capacitance, ending backward curve as the same value with forward curve at -5 V.

At parallel mode of CV measurement, the measuring capacitance at accumulation bias might be described as following[49]

$$C_{meas}{}^{-1} \propto (\frac{\varepsilon'_{eff,BTO}}{t_{BTO}})^{-1} + (\frac{\varepsilon'_{STO}}{t_{STO}})^{-1} \quad (1)$$

The $\varepsilon'_{eff,BTO}$ is the real part of BTO permittivity and ε'_{STO} is the real part of STO permittivity, which should be a constant since no ferroelectricity existed in cubic STO. The $t_{BTO,STO}$ are the BTO and STO thickness, respectively. Because the dipole polarizability of BTO can response below microwave

Accepted

frequency (~GHz) and the $t_{BTO,STO}$ is the same for all the samples, the C_{meas} at accumulation should represent the value of $\varepsilon'_{eff,BTO}$. Furthermore, it should also give the number of c-BTO dipoles because the (001)-axis electrical field only trigger the spontaneous polarization in c-BTO instead of a-BTO[50]. Since BTO is a ferroelectric material, the dielectric constant $\varepsilon'$is the largest at the coercive point, which is at +/-3 V in our device[51]. Based on the equation (1), the backward curve at coercive point (at -3 V) had larger $\varepsilon'_{eff,BTO}$ than the forward curve, resulting in a higher C_{meas}. Therefore, the capacitance difference values were linked with (001)-dipoles and were extracted in the Figure 5(d). As oxygen pressure increased, the capacitance difference was reduced, which also linked to the smaller hysteresis behavior in the Figure 5(b). Based on the C-V characteristics, the dielectric constant at low frequencies (i.e. 100k Hz) was extracted with an average value of 130, which was in good agreement with reported values of epitaxial BTO[52,53]. For the 0.05 mbar sample, even though it was mostly a-oriented from XRD result, the BTO close to STO layer with thickness around 20 nm was still c-oriented. Thus, the hysteresis loop was still measured but smaller than 0.01 mbar BTO due to the less dipoles along (001) direction. The BTO C-V curve can be nicely explained via dipole amount and direction, and showed good agreement with XRD results, is therefore an electrical demonstration of c- to a-transition with oxygen pressure variation.

DISCUSSION

Our experimental study showed that the growth conditions made a drastic impact on the structural and electrical properties of the BTO layers. XRD indicated that the dominant orientation of the BTO polarization could be changed from c- to a- by increasing the O_2 pressure. Due to the similar thickness between BTO samples, the peak position shift should only result from different degree of lattice mismatch relaxation inside the BTO thin films by changing growth parameters. In addition, the presence of sub-peaks in XRD plots of high and medium O_2 pressure samples suggested a non-uniform distribution of lattice inside these samples.

Accepted

NBD analysis revealed a mosaic structure of 3 samples and highlighted differences in the mosaicity between the samples. The low O_2 pressure sample had the largest domain size and also showed higher lattice mismatch than 2 other samples. We attributed accelerated relaxation process in the medium and high O_2 pressure samples to the reduction of the BTO domain size, which facilitated strain relaxation via domain formation[54]. With larger domain size inside the low O_2 pressure sample, the strain relaxation might be delayed compared with smaller domain size samples. The residual compressive strain in the low O_2 pressure sample produced elongation of the out-of-plane lattice parameter, favorizing growth of the c-BTO.

Observed differences in the grain size and strain relaxation could also be related to the growth mode change. As we increased the oxygen pressure, the BTO films tended to favor 3D growth, as shown in the AFM images in the Figure 3(d)-(f). BTO clusters appeared when oxygen pressure increased to 0.05 mbar. Difference in the growth mode also can explain observed difference in strain relaxation since formation of the misfit dislocations at the grain boundaries during 3D growth occurs easier than during 2D growth, which requires dislocation gliding.

Another possible explanation for the delayed strain relaxation of low oxygen pressure sample was the amount of oxygen vacancies. Oxygen vacancies inside perovskite systems were reported to have impact on strain relaxation behavior. In LaSrCoO (LSCO) material system, oxygen vacancies helped retain strain inside these perovskite oxide films by re-ordering on Co-O planes[55–57]. With this re-ordering, strain was not relaxed until even larger thickness was reached. In our BTO / STO / Si system, the strain behavior could be explained with the similar assumption. For samples grown with lower oxygen pressure, more oxygen vacancies were expected inside the as-deposited thin films. However, this oxygen vacancies re-ordering is not yet reported inside the BTO material, thus more studies would need to be carried out before making a solid conclusion.

Piezoelectric force microscopy (PFM) is a widely used technique for ferroelectricity characterization with the ability to analyze the domain and dipole behavior in the out-of-plane direction. However, for

Accepted

the in-plane domain, i.e., the a-BTO, the characterization is not feasible due to the perpendicular electric field direction with respect to the in-plane dipoles. Compared with PFM, C-V measurement is using similar concept by measuring charge differences in the BTO. In addition, we can further extract the dielectric constant from C-V curves, which is another indication of film quality and can also be linked with the optical indices.

The C-V hysteresis can be correlated with both charge defects and ferroelectric behavior of BTO films. However, the positively charged oxygen vacancies and the ferroelectricity result in different direction of hysteresis loop. In our C-V curve, the counterclockwise direction indicates that the ferroelectricity is more pronounced than charged defect. Thus, for our BTO films, it will be difficult to use C-V measurement for charged defect characterization.

Conclusion

In conclusion, we demonstrate an epitaxial BTO film growing on top STO / Si(001) pseudo-substrate by PLD technique. Adjusting oxygen pressure during growth results in polarization direction change. The lattice mismatch relaxation process is measured using XRD and confirmed by cross-sectional NBD analysis. By measuring electrical properties of ferroelectric BTO films, the hysteresis behavior is explained and again well-matched with XRD results.

Supplementary Material

See supplementary material for the additional XRD and C-V hysteresis results.

Acknowledgement

This research has received funding from the European Research Council (ERC) under the European Union's Horizon 2020 research and innovation program (grant agreement No.742299)

Data Availability Statement

Accepted

The data that support the findings of this study are available from the corresponding author upon reasonable request.

References

[1] X. Zhu, Z. Liu, and N. Ming, J. Mater. Chem. **20**, 4015 (2010).

[2] D. Panda and T.-Y. Tseng, Ferroelectrics **471**, 23 (2014).

[3] T. Yajima, Y. Hikita, and H.Y. Hwang, Nat. Mater. **10**, 198 (2011).

[4] C. Xiong, W.H.P. Pernice, J.H. Ngai, J.W. Reiner, D. Kumah, F.J. Walker, C.H. Ahn, and H.X. Tang, Nano Lett. **14**, 1419 (2014).

[5] D. Damjanovic, P. Muralt, and N. Setter, IEEE Sens. J. **1**, 191 (2001).

[6] A.J. Moulson and J.M. Herbert, Electroceramics 5 (2003).

[7] H.D. Megaw, Acta Crystallogr. **5**, 739 (1952).

[8] S. Abel, T. Stöferle, C. Marchiori, C. Rossel, M.D. Rossell, R. Erni, D. Caimi, M. Sousa, A. Chelnokov, B.J. Offrein, and J. Fompeyrine, Nat. Commun. **4**, 1671 (2013).

[9] C. Eisenschmidt, H.T. Langhammer, R. Steinhausen, and G. Schmidt, Ferroelectrics **432**, 103 (2012).

[10] A. Petraru, J. Schubert, M. Schmid, and C. Buchal, Appl. Phys. Lett. **81**, 1375 (2002).

[11] H.A. Lu, L.A. Wills, B.W. Wessels, W.P. Lin, and G.K. Wong, Appl. Phys. Lett. **63**, 874 (1993).

[12] K.J. Kormondy, Y. Popoff, M. Sousa, F. Eltes, D. Caimi, M.D. Rossell, M. Fiebig, P. Hoffmann, C. Marchiori, M. Reinke, M. Trassin, A.A. Demkov, J. Fompeyrine, and S. Abel,

Accepted

Nanotechnology **28**, 75706 (2017).

[13] S. Abel, F. Eltes, J.E. Ortmann, A. Messner, P. Castera, T. Wagner, D. Urbonas, A. Rosa, A.M. Gutierrez, D. Tulli, P. Ma, B. Baeuerle, A. Josten, W. Heni, D. Caimi, L. Czornomaz, A.A. Demkov, J. Leuthold, P. Sanchis, and J. Fompeyrine, Nat. Mater. **18**, 42 (2019).

[14] L. Mazet, S.M. Yang, S. V. Kalinin, S. Schamm-Chardon, and C. Dubourdieu, Sci. Technol. Adv. Mater. **16**, 36005 (2015).

[15] M. Scigaj, C.H. Chao, J. Gázquez, I. Fina, R. Moalla, G. Saint-Girons, M.F. Chisholm, G. Herranz, J. Fontcuberta, R. Bachelet, and F. Sánchez, Appl. Phys. Lett. **109**, 122903 (2016).

[16] R.W. Boyd, in *Nonlinear Opt.*, edited by R.W.B.T.-N.O. (Third E. Boyd (Academic Press, Burlington, 2008), pp. 511–541.

[17] P. Castera, D. Tulli, A.M. Gutierrez, and P. Sanchis, Opt. Express **23**, 15332 (2015).

[18] V. Vaithyanathan, J. Lettieri, W. Tian, A. Sharan, A. Vasudevarao, Y.L. Li, A. Kochhar, H. Ma, J. Levy, P. Zschack, J.C. Woicik, L.Q. Chen, V. Gopalan, and D.G. Schlom, J. Appl. Phys. **100**, 24108 (2006).

[19] C. Schmitz-Antoniak, D. Schmitz, P. Borisov, F.M.F. de Groot, S. Stienen, A. Warland, B. Krumme, R. Feyerherm, E. Dudzik, W. Kleemann, and H. Wende, Nat. Commun. **4**, 2051 (2013).

[20] S.-H. Baek and C.-B. Eom, Acta Mater. **61**, 2734 (2013).

[21] R. Droopad, Z. Yu, H. Li, Y. Liang, C. Overgaard, A. Demkov, X. Zhang, K. Moore, K. Eisenbeiser, M. Hu, J. Curless, and J. Finder, J. Cryst. Growth **251**, 638 (2003).

[22] C. Merckling, G. Saint-Girons, C. Botella, G. Hollinger, M. Heyns, J. Dekoster, and M.

Accepted

Caymax, Appl. Phys. Lett. **98**, 92901 (2011).

[23] H. Guo, D. Sun, W. Wang, Z. Gai, I. Kravchenko, J. Shao, L. Jiang, T.Z. Ward, P.C. Snijders, L. Yin, J. Shen, and X. Xu, J. Appl. Phys. **113**, 234301 (2013).

[24] G. Koster, G.J.H.M. Rijnders, D.H.A. Blank, and H. Rogalla, Appl. Phys. Lett. **74**, 3729 (1999).

[25] H.M. Christen and G. Eres, J. Phys. Condens. Matter **20**, 264005 (2008).

[26] P.G. Sundell, M.E. Björketun, and G. Wahnström, Phys. Rev. B - Condens. Matter Mater. Phys. **73**, 104112 (2006).

[27] H.N. Lee, S.S. Ambrose Seo, W.S. Choi, and C.M. Rouleau, Sci. Rep. **6**, 19941 (2016).

[28] E. Hildebrandt, J. Kurian, M.M. Mller, T. Schroeder, H.J. Kleebe, and L. Alff, Appl. Phys. Lett. **99**, 112902 (2011).

[29] J. Seidel, P. Maksymovych, Y. Batra, A. Katan, S.Y. Yang, Q. He, A.P. Baddorf, S. V. Kalinin, C.H. Yang, J.C. Yang, Y.H. Chu, E.K.H. Salje, H. Wormeester, M. Salmeron, and R. Ramesh, Phys. Rev. Lett. **105**, 197603 (2010).

[30] M.E. Zvanut, S. Jeddy, E. Towett, G.M. Janowski, C. Brooks, and D. Schlom, J. Appl. Phys. **104**, 64122 (2008).

[31] H.Y. Xu, Y.H. Huang, S. Liu, K.W. Xu, F. Ma, and P.K. Chu, RSC Adv. **6**, 79383 (2016).

[32] B.J. Fishbein, J. Electrochem. Soc. **134**, 674 (1987).

[33] S. Choi, K.H. Min, M.S. Jeong, J.I. Lee, M.G. Kang, H.-E. Song, Y. Kang, H.-S. Lee, D. Kim, and K.-H. Kim, Sci. Rep. **7**, 12853 (2017).

[34] T. Tambo, T. Nakamura, K. Maeda, H. Ueba, and C. Tatsuyama, Jpn. J. Appl. Phys. **37**, 4454

Accepted

(1998).

[35] M. Spreitzer, D. Klement, R. Egoavil, J. Verbeeck, J. Kovač, A. Založnik, G. Koster, G. Van Tendeloo, D. Suvorov, and G. Rijnders, J. Mater. Chem. C **8**, 518 (2020).

[36] C. Merckling, M. Korytov, U. Celano, M.-H.M. Hsu, S.M. Neumayer, S. Jesse, and S. de Gendt, J. Vac. Sci. Technol. A **37**, 21510 (2019).

[37] F. Niu and B.W. Wessels, J. Vac. Sci. Technol. B Microelectron. Nanom. Struct. Process. Meas. Phenom. **25**, 1053 (2007).

[38] M.-H.M. Hsu, A. Marinelli, C. Merckling, M. Pantouvaki, J. Van Campenhout, P. Absil, and D. Van Thourhout, Opt. Mater. Express **7**, 2030 (2017).

[39] J.M. Cowley, Ultramicroscopy **90**, 197 (2002).

[40] P. Favia, M. Bargallo Gonzales, E. Simoen, P. Verheyen, D. Klenov, and H. Bender, J. Electrochem. Soc. **158**, H438 (2011).

[41] D. Cooper, T. Denneulin, N. Bernier, A. Béché, and J.-L. Rouvière, Micron **80**, 145 (2016).

[42] J.Z. Tischler, G. Eres, B.C. Larson, C.M. Rouleau, P. Zschack, and D.H. Lowndes, Phys. Rev. Lett. **96**, 226104 (2006).

[43] H. Schraknepper, C. Bäumer, F. Gunkel, R. Dittmann, and R.A. De Souza, APL Mater. **4**, 126109 (2016).

[44] C.W. Schneider and T. Lippert, in *Laser Process. Mater.*, edited by P. Schaaf (Springer Berlin Heidelberg, Berlin, Heidelberg, 2010), pp. 89–112.

[45] M.-H.M. Hsu, D. Van Thourhout, M. Pantouvaki, J. Meersschaut, T. Conard, O. Richard, H. Bender, P. Favia, M. Vila, R. Cid, J. Rubio-Zuazo, G.R. Castro, J. Van Campenhout, P. Absil,

Accepted

and C. Merckling, Appl. Phys. Express **10**, 65501 (2017).

[46] J. Lyu, S. Estandía, J. Gazquez, M.F. Chisholm, I. Fina, N. Dix, J. Fontcuberta, and F. Sánchez, ACS Appl. Mater. Interfaces **10**, 25529 (2018).

[47] M. Scigaj, N. Dix, I. Fina, R. Bachelet, B. Warot-Fonrose, J. Fontcuberta, and F. Sánchez, Appl. Phys. Lett. **102**, 112905 (2013).

[48] O. Trithaveesak, J. Schubert, and C. Buchal, J. Appl. Phys. **98**, 114101 (2005).

[49] J. Tao, C.Z. Zhao, C. Zhao, P. Taechakumput, M. Werner, S. Taylor, and P.R. Chalker, Materials (Basel). **5**, 1005 (2012).

[50] D.J. Griffiths, in *Introd. to Electrodyn.*, edited by D.J. Griffiths, 4th ed. (Cambridge University Press, Cambridge, 2019), pp. 167–209.

[51] D. Damjanovic, Reports Prog. Phys. **61**, 1267 (1998).

[52] G. Niu, B. Gautier, S. Yin, G. Saint-Girons, P. Lecoeur, V. Pillard, G. Hollinger, and B. Vilquin, Thin Solid Films **520**, 4595 (2012).

[53] V. Srikant, E.J. Tarsa, D.R. Clarke, and J.S. Speck, J. Appl. Phys. **77**, 1517 (1995).

[54] B.S. Kwak, A. Erbil, J.D. Budai, M.F. Chisholm, L.A. Boatner, and B.J. Wilkens, Phys. Rev. B **49**, 14865 (1994).

[55] J. Gazquez, S. Bose, M. Sharma, M.A. Torija, S.J. Pennycook, C. Leighton, and M. Varela, APL Mater. **1**, 12105 (2013).

[56] J. Gazquez, W. Luo, M.P. Oxley, M. Prange, M.A. Torija, M. Sharma, C. Leighton, S.T. Pantelides, S.J. Pennycook, and M. Varela, Nano Lett. **11**, 973 (2011).

[57] D.O. Klenov, W. Donner, B. Foran, and S. Stemmer, Appl. Phys. Lett. **82**, 3427 (2003).

Accepted

Figure captions

Figure 1. Symmetric XRD ω-2θ scan of samples with (a) different growth rate and (b) different substrate temperature. The arrow indicates the shoulder sub-peak position. The dashed and solid lines represent bulk tetragonal BTO(002) and BTO(200) position, respectively. All the peak positions are calibrated using Si(004) peak. (c) The FWHM derived from the (002) ω-scan BTO peak of samples grown by different growth rate and substrate temperature.

Figure 2. (a) Symmetric XRD ω-2θ scan of samples under different oxygen pressure. (b)-(d) Deconvolution of BTO(002) peak with O_2 pressure of 0.01, 0.025, and 0.05 mbar. (e) Peak area percentage of the deconvoluted peaks. The lattice parameters are calculated by the XRD peak positions using Bragg's law.

Figure 3. Cross-sectional NBD maps of in-plane lattice mismatch of (a) c-BTO (b) mixed BTO and (c) a-BTO films calculated with the reference region in BTO. AFM surface morphology of (d) c-BTO (e) mixed BTO and (f) a-BTO films.

Figure 4. Cross-sectional NBD maps of out-of-plane lattice mismatch of (a) c-BTO (b) mixed BTO and (c) a-BTO films calculated with the reference region in BTO. The averaged lattice mismatch profiles normalized to the STO buffer layer lattice parameter of (d) in-plane and (e) out-of-plane direction.

Figure 5. (a) Current-voltage curve of 0.01 mbar BTO sample under different voltage biases. Ferroelectric behavior was not shown until applied voltage larger than +/- 3 V. (b) Normalized Capacitance-voltage curve at 1M Hz of different oxygen pressure samples. The larger the oxygen

Accepted

pressure, the smaller the hysteresis loop observed. (c) The schematic C-V curve, with detailed BTO dipole polarization and STO / p^{+}Si interface charged state being plotted. Insertion is multi-frequency CV measurement from 1k to 100k Hz, which shows a clear inversion layer formation with fixed value of accumulation capacitance. (d) The difference between forward and backward accumulation capacitance for different oxygen pressure samples.

Accepted

Figure 1

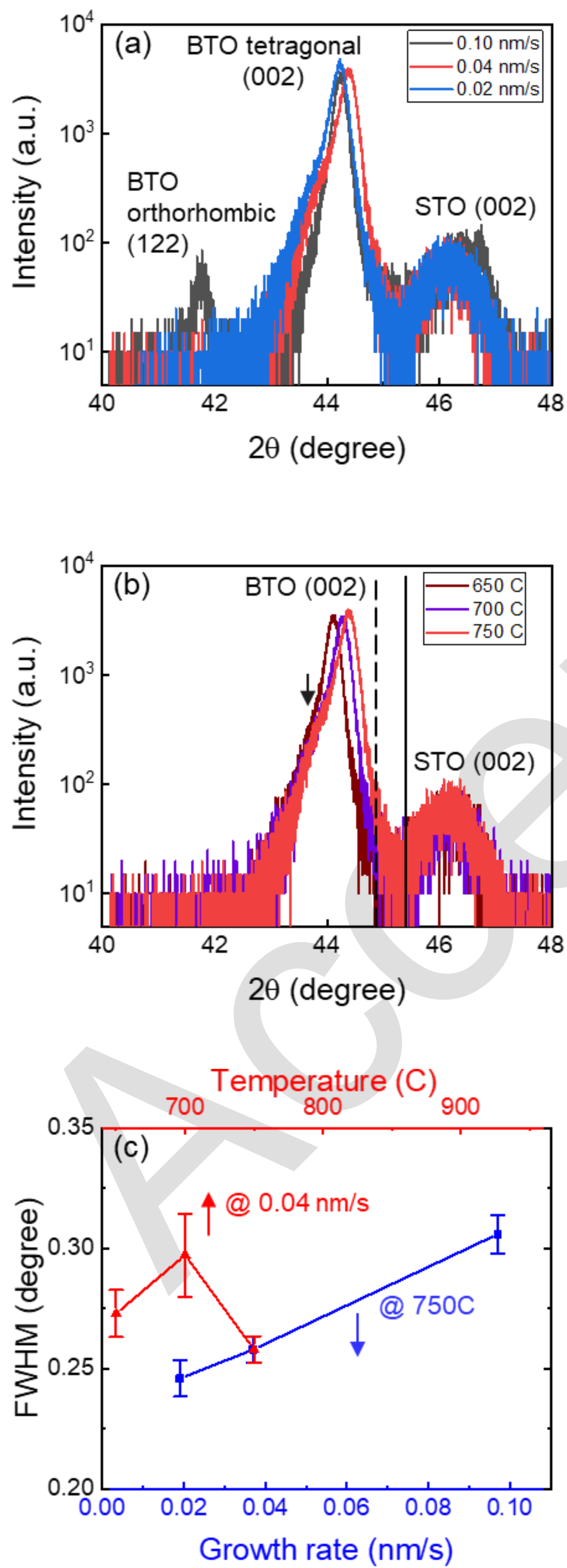

Accepted

Figure 2

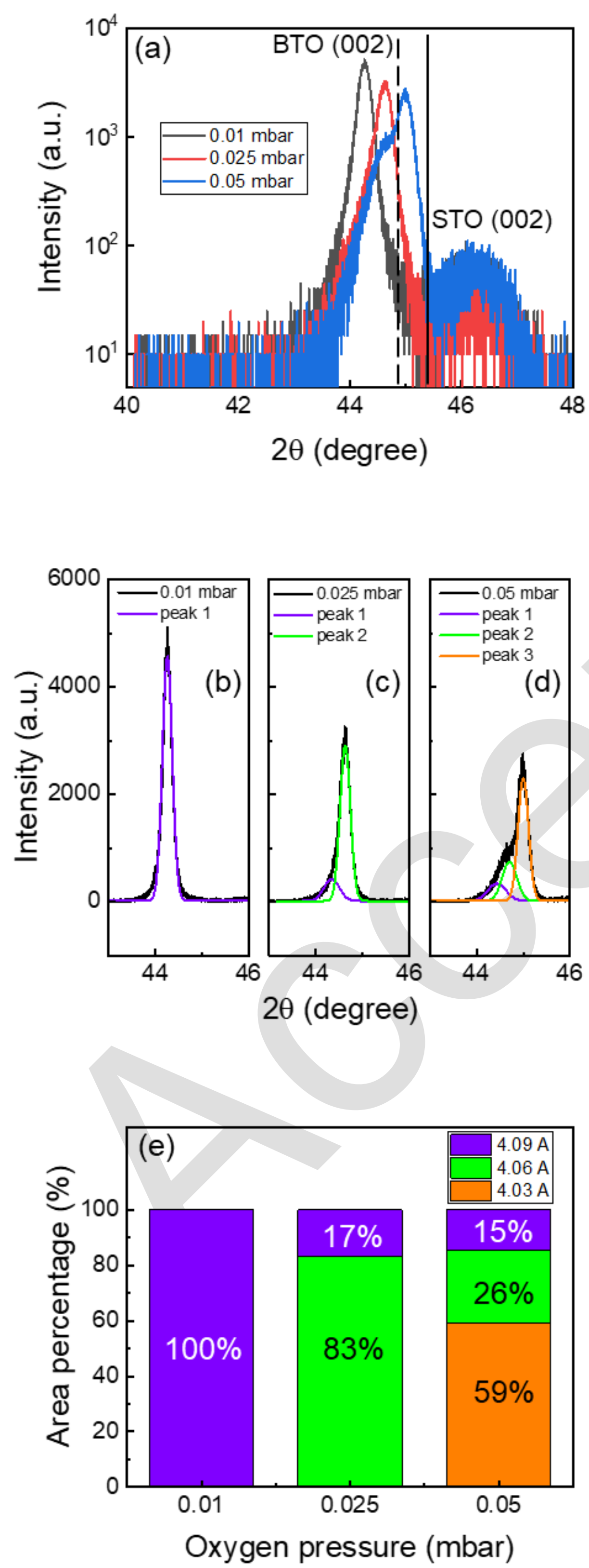

Accepted

Figure 3

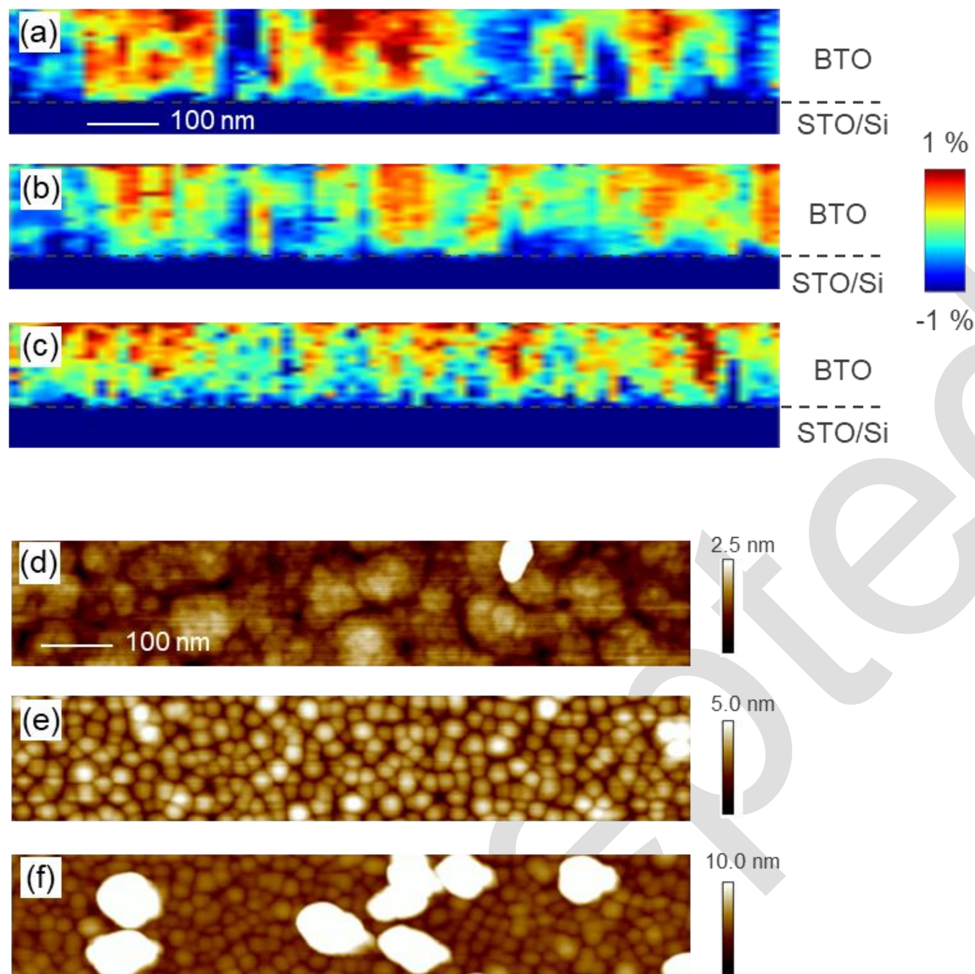

Accepted

Figure 4

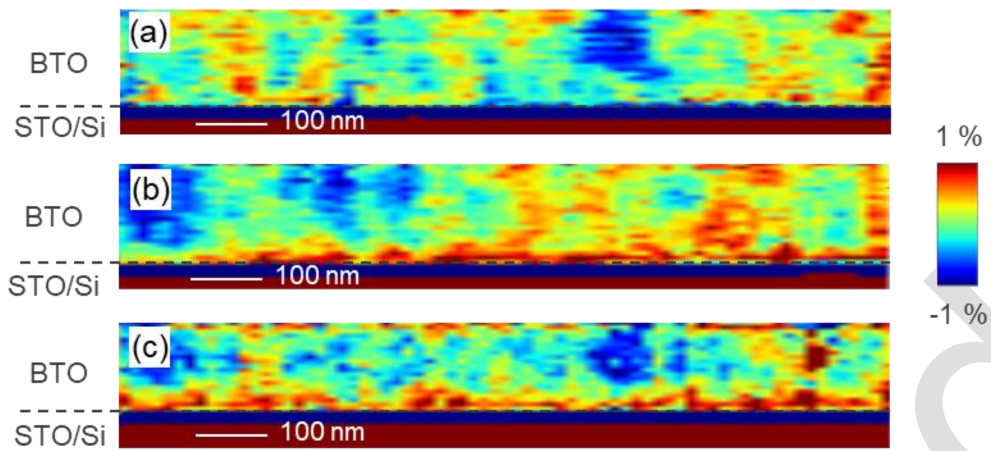

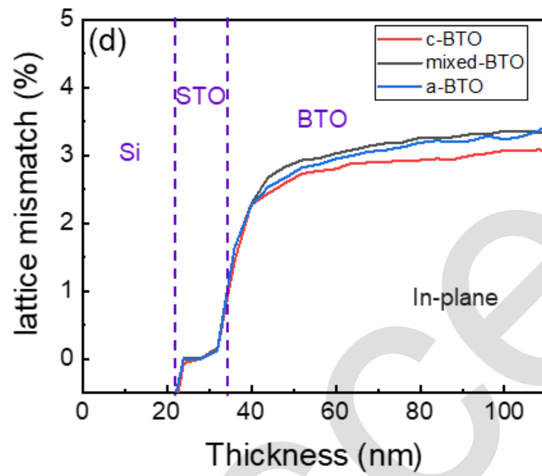

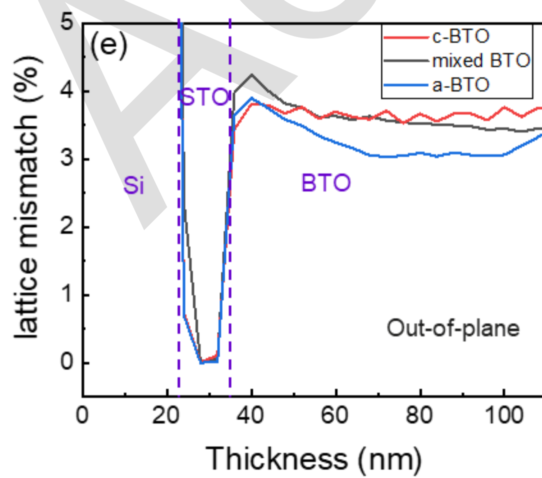

Accepted

Figure 5

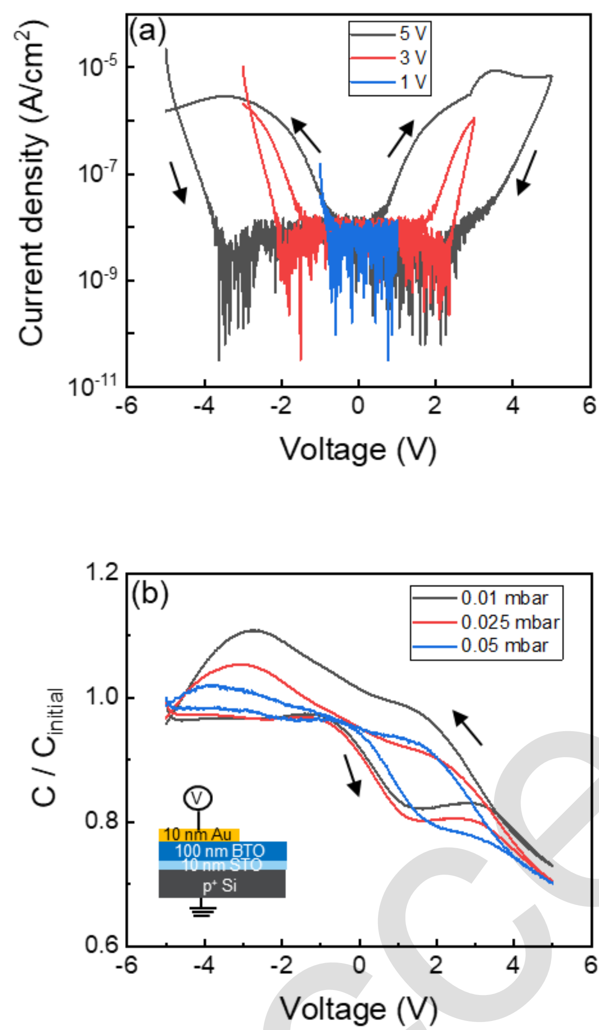

Accepted

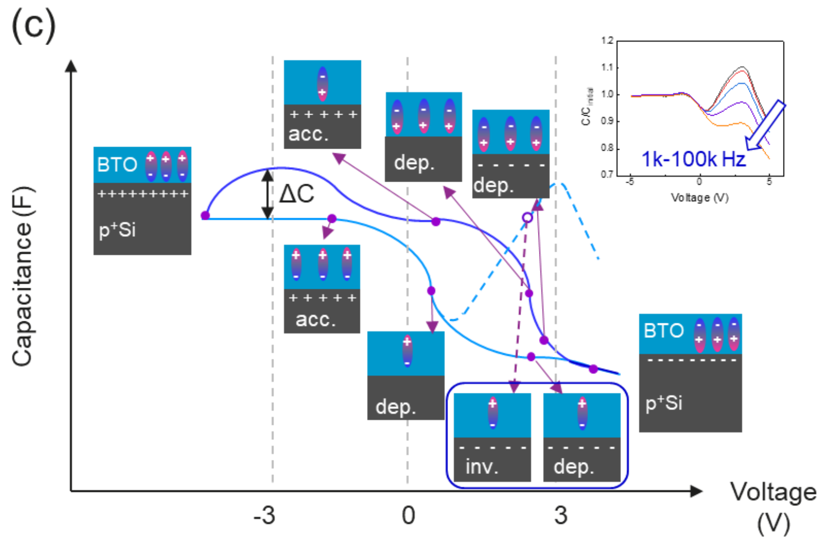

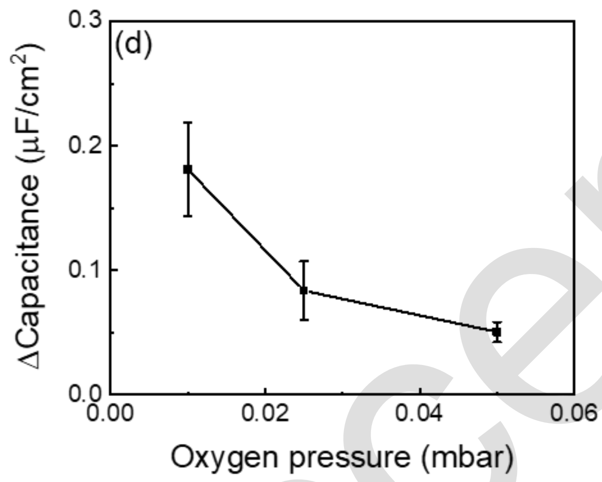

Accepted

Supplementary information

Polarization control of epitaxial barium titanate ($BaTiO_3$) grown by Pulsed-Laser Deposition on a MBE-$SrTiO_3$/Si(001) pseudo-substrate

Tsang-Hsuan Wang[1,2,*], Po-Chun (Brent) Hsu[1,3], Maxim Korytov[1], Jan Genoe[1,2] and Clement Merckling[1]

1: Imec, Kapeldreef 75, B-3001 Leuven, Belgium

2: ESAT Department, KU Leuven, Kasteelpark Arenberg 10, B-3001 Leuven, Belgium

3: Department of Materials Engineering, KU Leuven, Kasteelpark Arenberg 44, B-3001 Leuven, Belgium

*e-mail: tsang.hsuan.wang@imec.be

Accepted

Supplementary Figures

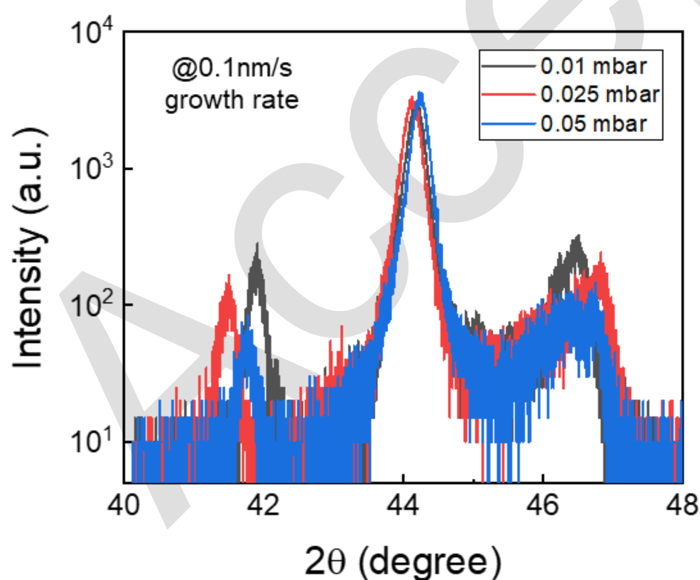

Supplementary Figure S1 – Polycrystalline BTO using large growth rate of 0.1nm/s

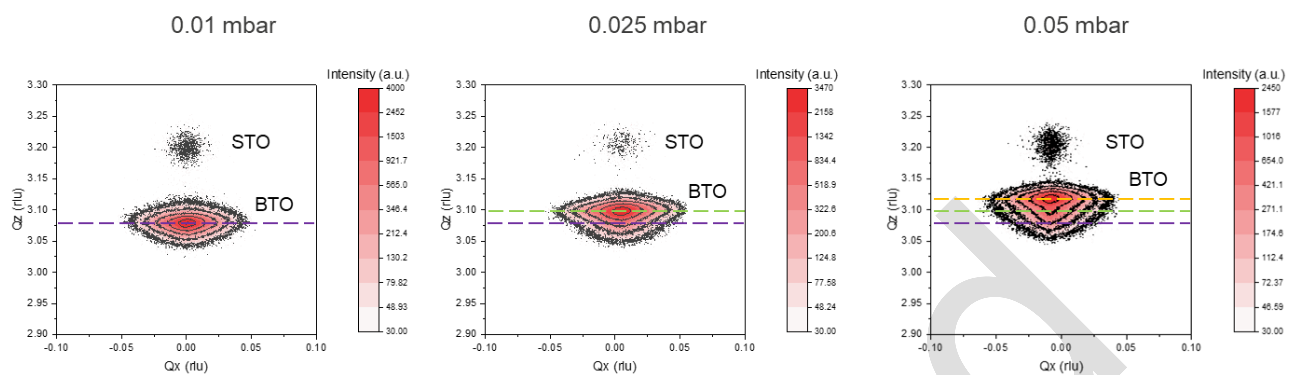

Supplementary Figure S2 – RSM results of different oxygen pressure BTO films. The BTO contour becomes asymmetric as the oxygen pressure increases, indicating the presence of shoulder sub-peaks.

Accepted

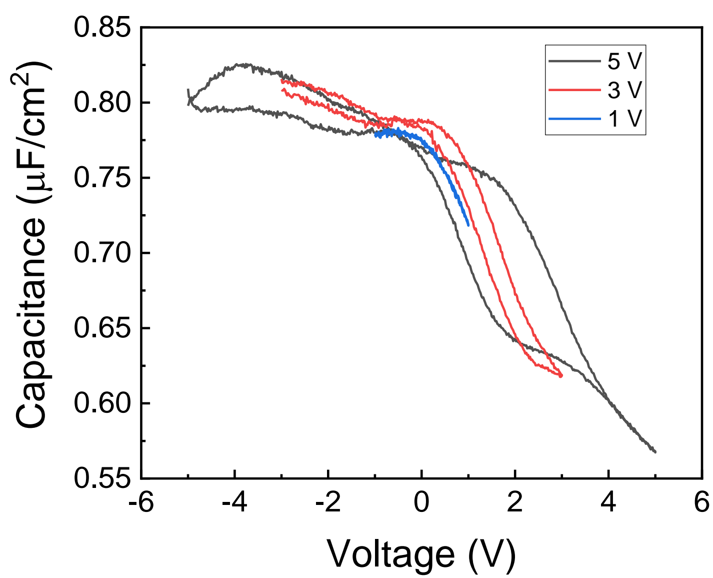

Supplementary Figure S3 – Different voltage windows for C-V measurement at 1M Hz. The C-V curve with voltage larger than 3V shows hysteresis behavior, which is similar to the I-V behavior.

Accepted

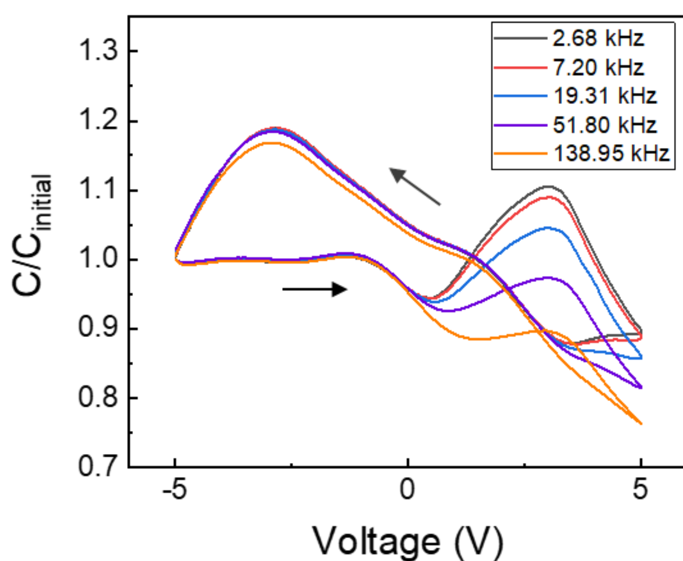

Supplementary Figure S4 – Hysteresis C-V curves under different frequencies. As the frequency increased to larger than 100 kHz, inversion capacitance is no longer observable.

The drop of capacitance in the inversion region larger than +3 V can be explained by the dipole formation (polarized down as shown in manuscript Fig. 5c). As the dipole forms, the reversed charged direction results in the decrease of total charge at insulator/Si interface. By the definition of capacitance, where

$$C = \frac{dQ}{dV}$$

As the dQ is decreasing, the measured C is thus decreasing.

Accepted

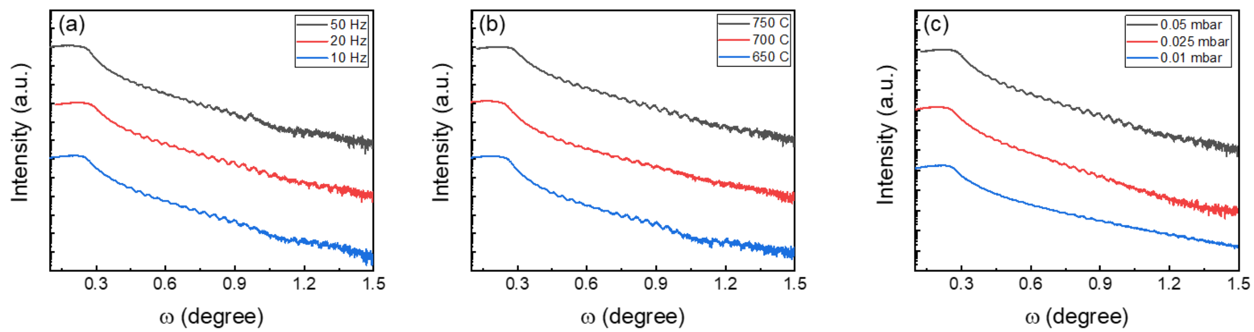

Supplementary Figure S5 – XRR curves of (a) different repetition rates (b) different temperatures and (c) different oxygen pressures

Accepted

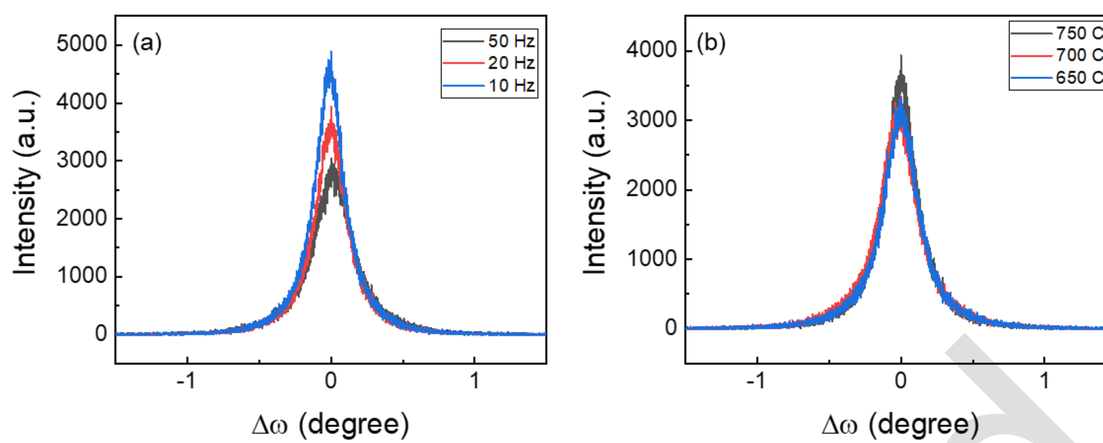

Supplementary Figure S6 – omega scans of (a) different repetition rate and (b) different temperature BTO samples

Accepted

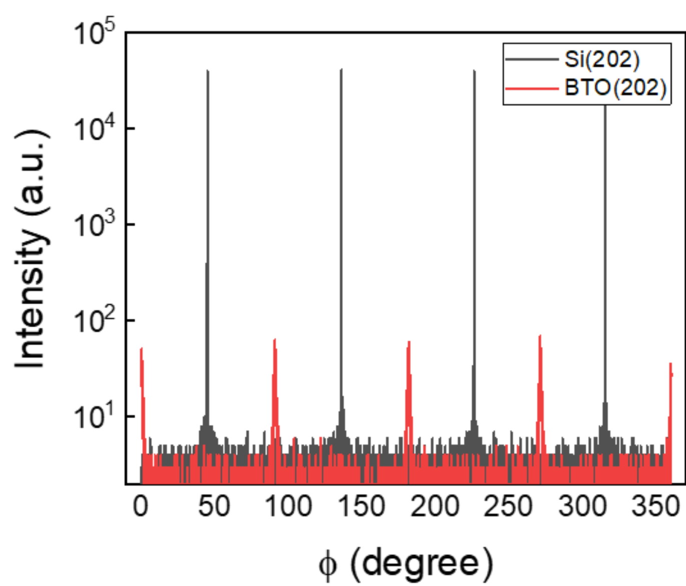

Supplementary Figure S7 – phi scans of BTO(202) and Si(202) of 0.05 mbar BTO sample

Accepted